Supplementary information

BNNT vs CNT: Influence of Structural Defects on Damping Characteristics of Nanocomposites

Taeho Lee[1], Jun-Sik Kim[2] and Seunghwa Yang[2*]

[1]*Department of Energy Systems Engineering, Chung-Ang University, 84 Heukseok-Ro, Dongjak-Gu, Seoul 06974, South Korea*

[2]*Department of Mechanical System Engineering, Kumoh National Institute of Technology, 61 Daehak-Ro, Gumi , Kyeongbuk 39177, South Korea*

[*] *Corresponding Author: Email- fafala@cau.ac.kr; Tel.: +82-2-820-5266*

Supplementary S1: Molecular modelling and ensemble simulation procedures

In this study, a commercially available molecular dynamics simulation program Software for Chemistry & Materials (SCM), was used for preparation and ensemble simulation of the molecular unit-cell models of the PEEK matrix, nanotubes, and nanocomposites. To describe all the inter- and intra-atomic interactions during cell construction, equilibration, and production runs, the reactive force field ReaxFF was used as follows [1]:

$$E_{system} = E_{bond} + E_{over} + E_{angle} + E_{torsion} + E_{vdW} + E_{coulomb} + E_{specific} \quad (1)$$

E_{bond}, E_{angle}, and $E_{torsion}$ are the potential energies associated with bond-stretching, angle-bending, and torsion-dihedral change of the primarily bonded structures, respectively. E_{over} denotes an energy penalty that prevents the over-coordination of atoms. $E_{coulomb}$ and E_{vdW} are the electrostatic and van der Waals energies between noncovalently interacting atoms, respectively. $E_{specific}$ is the energy associated with specific terms such as conjugation,

hydrogen bond, and C_2 correction. The complete functional forms and potential parameters are available in the supplementary information section of the original paper reporting the development of ReaxFF for gas-phase h-BN nanostructure synthesis [2].

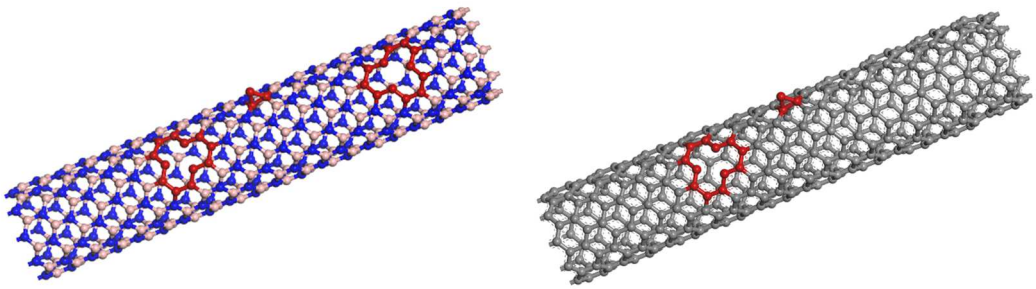

(a) (b)

Fig. S1-1. Models of defect-containing nanotubes: (a) BNNT and (b) CNT defects.

Both CNT and BNNT were modelled as chiral single-walled nanotubes with a chiral index of (10, 0). Using the pristine nanotube as a reference, five and ten vacancies and oxidation defects, respectively, were randomly generated on the nanotube surface, as shown in Fig. S1-1. In CNTs, oxidation defects are formed by covalently bonding one oxygen atom to two carbon atoms, thereby forming an epoxide group. In BNNTs, oxidation defects are formed when one oxygen atom is bonded to neighbouring B and N atoms. When the defects are structurally aligned, for example, along the longitudinal axis, the resultant interfacial stick-slip can be altered. Considering the fact that the local curvature formed around defects in the nanotube or graphene is a critical factor for interfacial load transfer, the spatial ordering of the position of defects can result in a maximized or minimized stick-slip mechanism. We aim to study the optimization of the defect type and arrangement in future.

Amorphous PEEK was used as the matrix material. After the nanotubes and PEEK matrix were constructed independently, geometry optimisation was implemented using the conjugate gradient method to minimise the total potential energy of the systems. To construct the nanocomposites, each nanotube was embedded at the centre of a PEEK unit cell without

involving covalent grafting between the tube and matrix. The nanocomposite unit cells were geometrically optimised again using the conjugate gradient method. Subsequently, equilibration was conducted at 300 K and 1 atm using the *NPT* ensemble: isothermal and isobaric simulations were implemented using the Nosé–Hoover thermostat and Berendsen barostat, respectively, for 500 ps with a time integration step of 0.25 fs [3–4]. Periodic boundary conditions were applied to the nanocomposites; therefore, the nanotubes in the longitudinal direction of the nanocomposite unit-cell were infinitely long. The details of the nanocomposite unit-cell compositions are summarised in Table S1-1.

Table S1-1. Composition of the nanocomposites after equilibration at 300 K and 1 atm for 500 ps.

		#of defects	Volume fraction	Nanocomposites					
				X (Å)	Y (Å)	Z (Å)	Density (g/cm^3)	ρ_v	ρ_o
BNNT	Pristine	0	5%	41.001	39.398	44.171	1.324	0	0
	B vacancy	5	5%	41.553	40.722	43.467	1.283	0.0125	-
		10	5%	42.637	39.911	43.518	1.273	0.0250	-
	N vacancy	5	5%	42.081	40.676	43.508	1.267	0.0125	-
		10	5%	40.906	42.155	43.342	1.261	0.0250	-
	Oxidation	5	5%	41.319	40.689	43.507	1.293	-	0.0250
		10	5%	41.418	41.139	43.697	1.272	-	0.0500
CNT	Pristine	0	5%	42.509	39.997	43.147	1.283	0	-
	C vacancy	5	5%	41.799	40.675	43.436	1.273	0.0125	-
		10	5%	41.754	40.788	43.561	1.266	0.0250	-
	Oxidation	5	5%	41.448	41.361	43.182	1.273	-	0.0250
		10	5%	42.707	39.878	43.162	1.284	-	0.0500

Supplementary S2: Viscoelastic properties production run and results

Once all nanocomposite unit cells were prepared, sinusoidal wiggling was applied with a predefined angular frequency varying from 1 GHz to 100 GHz through a microcanonical (NVE) simulation. Fig. S2-1 shows representative applied sinusoidal strain and resultant stress along the transverse direction of the nanocomposites, with the amplitude regulated to define the phase lag. The blue dots represent the discrete stress values, which were fitted to a sinusoidal form assuming that the resulting transverse stress is periodic. The amplitude of the stress was determined using the least-squares approximation. As shown in Figure S2-1, a clear phase lag δ can be observed between the applied strain and resulting stress. Therefore, the viscoelastic properties can be derived from the amplitude of the applied strain (ε_0), stress (σ_0), and the phase lag δ as shown below.

$$E' = \frac{\sigma_0}{\varepsilon_0}\sin\delta \tag{2}$$

$$E'' = \frac{\sigma_0}{\varepsilon_0}\cos\delta \tag{3}$$

$$\tan\delta = \frac{E''}{E'} \tag{4}$$

E', E'', and $\tan\delta$ denote the storage modulus, loss modulus, and loss tangent along the transverse direction of the nanocomposite, respectively.

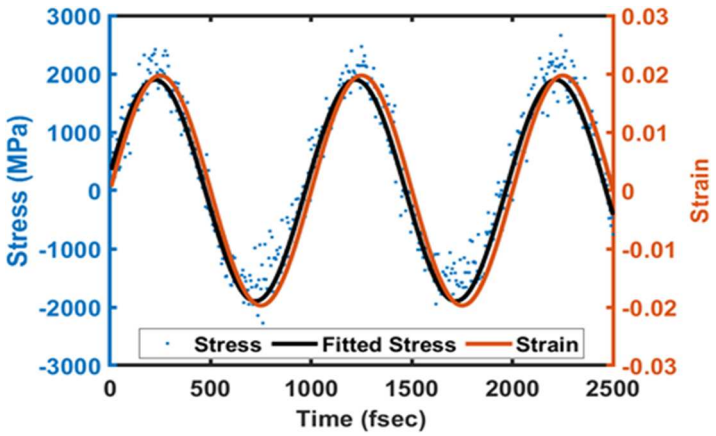

Fig. S2-1. Time evolution of the applied sinusoidal strain (orange), the resultant stress (discrete blue dots), and the sinusoidal stress (black) fitted from the least square approximation of the stress values.

The storage and loss moduli of the nanocomposites are shown in Figs. S2-2 and S3.

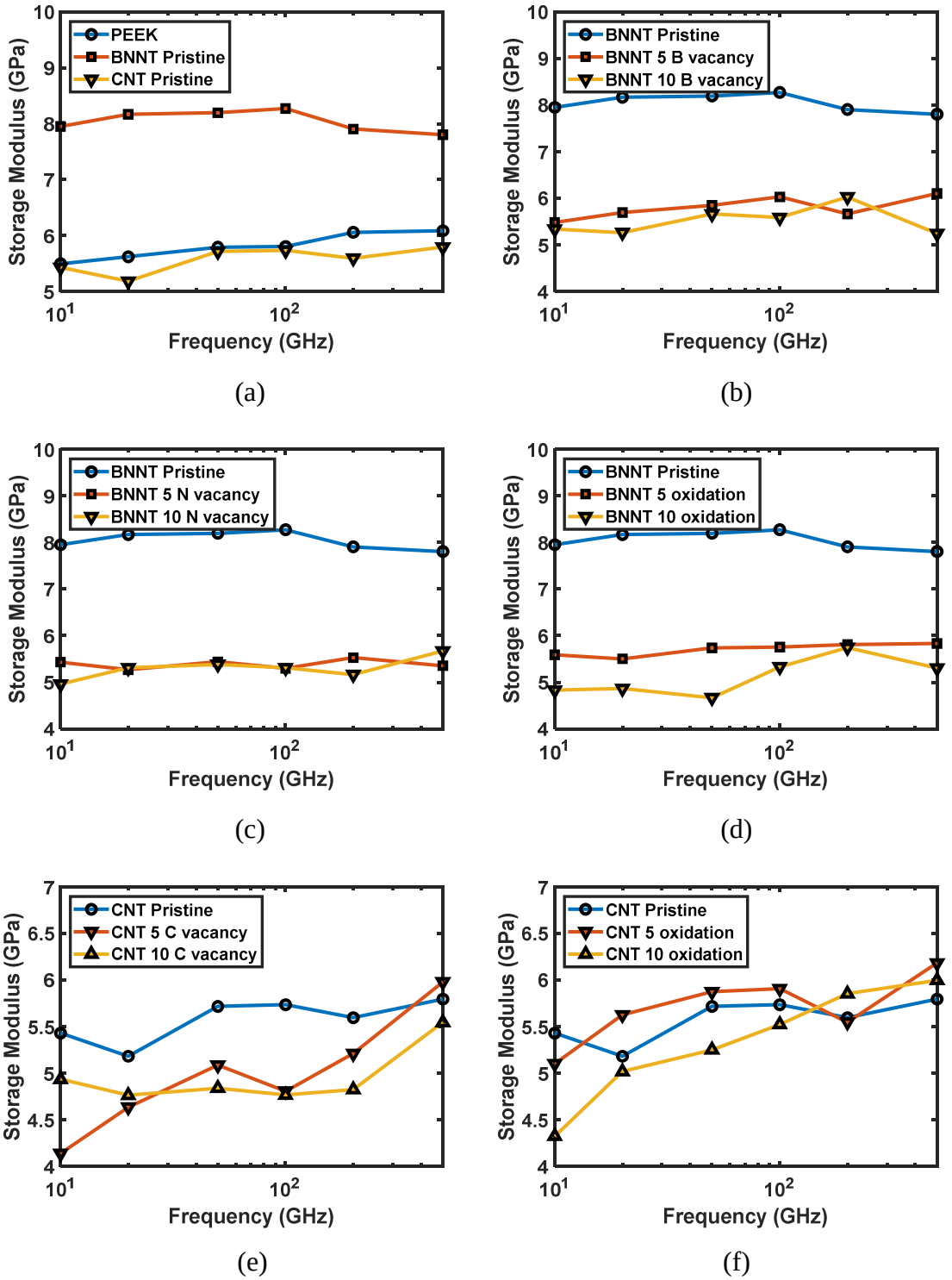

Fig. S2-2. Storage modulus of nanocomposites with (a) pristine BNNT and CNT, (b) BNNT containing boron vacancy defect, (c) BNNT containing nitrogen vacancy defect, (d) BNNT containing oxidation defect, (e) CNT containing carbon vacancy, and (f) CNT containing oxidation defect.

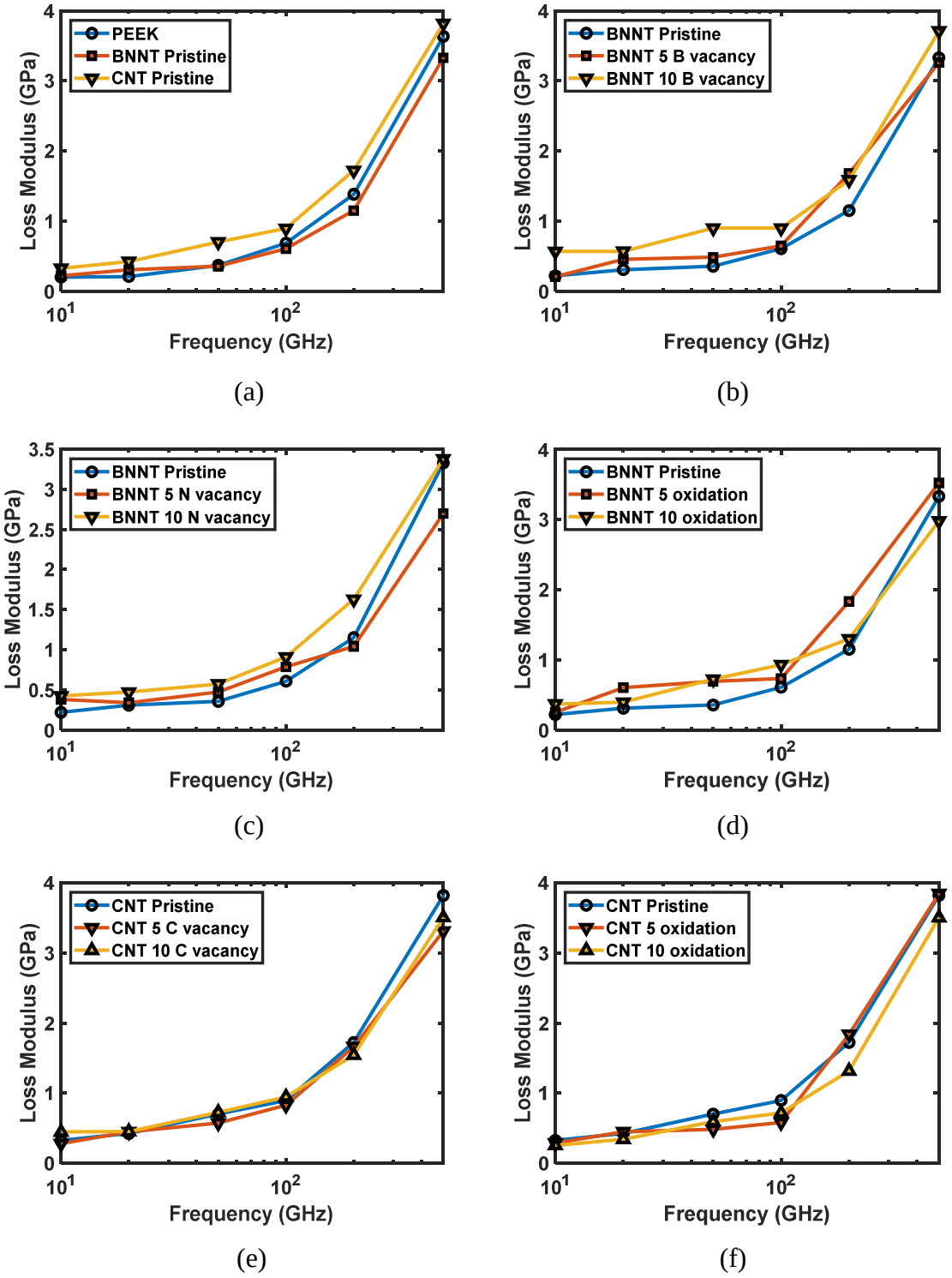

Fig. S2-3. Loss Modulus of nanocomposites with (a) pristine BNNT and CNT, (b) BNNT containing boron vacancy defect, (c) BNNT containing nitrogen vacancy defect, (d) BNNT containing oxidation defect, (e) CNT containing carbon vacancy, and (f) CNT containing oxidation defect.

Table S2-1. Average of the loss tangent of PPEK and nanocomposites.

Frequency (GHz)	10	20	50	100	200	500
PEEK	0.0367	0.0369	0.0642	0.1218	0.2296	0.6021
Composites BNNT	0.0277	0.0375	0.0433	0.0735	0.1458	0.4138
Composites CNT	0.0511	0.0844	0.1137	0.1558	0.3147	0.6219
Composites BNNT-5B	0.0449	0.0824	0.0821	0.1074	0.3070	0.5537
Composites BNNT-10B	0.1084	0.1054	0.1569	0.1611	0.2631	0.7088
Composites BNNT-5N	0.0737	0.0582	0.1047	0.1548	0.2045	0.5080
Composites BNNT-10N	0.0860	0.0852	0.1054	0.1848	0.2879	0.5643
Composites BNNT-5ox	0.0533	0.1167	0.1351	0.1371	0.3050	0.5915
Composites BNNT-10ox	0.0742	0.0954	0.1543	0.1743	0.2697	0.5903
Composites CNT-5C	0.0646	0.1030	0.1132	0.1641	0.3219	0.5434
Composites CNT-10C	0.0900	0.0939	0.1656	0.1688	0.3349	0.6689
Composites CNT-5ox	0.0835	0.0802	0.0841	0.1059	0.3313	0.6218
Composites CNT-10ox	0.0671	0.0708	0.1212	0.1368	0.2733	0.5842

Table S2-2. Standard deviation of the loss tangent of PPEK and nanocomposites.

Frequency (GHz)	10	20	50	100	200	500
PEEK	0.0143	0.0174	0.0186	0.0076	0.0525	0.0826
Composites BNNT	0.0020	0.0044	0.00261	0.0023	0.0107	0.0609
Composites CNT	0.0094	0.0098	0.0131	0.0237	0.0225	0.0717
Composites BNNT-5B	0.0230	0.0275	0.0111	0.0261	0.0113	0.0732
Composites BNNT-10B	0.0249	0.0152	0.0414	0.0052	0.0114	0.0240
Composites BNNT-5N	0.0195	0.0283	0.0416	0.0570	0.0468	0.0678
Composites BNNT-10N	0.0469	0.0135	0.0468	0.0503	0.0595	0.0511
Composites BNNT-5ox	0.0215	0.0294	0.0603	0.0245	0.0494	0.0391
Composites BNNT-10ox	0.0320	0.0590	0.1023	0.0113	0.0868	0.0553
Composites CNT-5C	0.0269	0.0150	0.0223	0.0428	0.0597	0.1145
Composites CNT-10C	0.0571	0.0506	0.0640	0.0433	0.0399	0.0489
Composites CNT-5ox	0.0408	0.0190	0.0222	0.0184	0.0280	0.0455
Composites CNT-10ox	0.0305	0.0133	0.0490	0.0440	0.0826	0.0073

Supplementary S3: Interface/interphase characterization and structural analysis

The thickness, amplitude (peak density), and average density of the interphase zone were defined using the radial density distribution of the PEEK molecules around the nanotubes. The thickness of the interface zone was determined from the distance between two points of uniform PEEK density (black dotted line) and radial distribution function (RDF), as shown in Fig. 3(a–b). The maximum RDF-profile peak around the nanotubes was considered the amplitude, and the average density of the interphase zone was determined as follows.

$$\rho_{avg} = \frac{1}{t_{int}} \int_0^{t_{int}} \rho(r)\, dr\,, \tag{5}$$

where t_{int} is the thickness of the interphase determined as mentioned above, and *r* is the radial coordinate from the centroid of the nanotubes. Several approaches have been reported in previous studies [5–7] for determining the interphase-zone properties.

The peak and average densities of the PEEK interphase around the BNNT decreased as vacancies and oxidation defects were introduced, whereas the width of the interphase increased (Table S3-1). The decrease in the interphase zone density indicates that the elasticity of the entire PEEK matrix decreased, contributing to the internal friction of the nanocomposites. Therefore, the defect-induced increase in the loss tangent of the BNNT/PEEK composites could be attributed to the softening of the interphase zone. However, the peak and average values of the interphase density around the CNT were not significantly affected by the defects in the CNT. Therefore, the interface/interphase of the nanocomposites played a significant role in determining the damping characteristics of the BNNT/PEEK nanocomposites, whereas its effect on the viscoelasticity of the CNT/PEEK nanocomposites was relatively insignificant.

Table S3-1. Thickness, peak density, and average density of interphase zone in the nanocomposites

Nanotube	Defects	Interphase Thickness (Å)	Peak Density (g/cm^3)	Average Density (g/cm^3)
BNNT	Pristine	1.797	2.641	1.973
	5 B vacancy	1.942	2.238	1.937
	10 B vacancy	2.217	2.033	1.809
	5 N vacancy	2.222	2.228	1.897
	10 N vacancy	1.843	2.437	1.810
	5 Oxidation	2.192	2.064	1.943
	10 Oxidation	2.169	2.081	1.789
CNT	Pristine	2.687	2.529	2.099
	5 C vacancy	2.633	2.426	2.071
	10 C vacancy	2.659	2.502	2.069
	5 Oxidation	3.000	2.217	1.885
	10 Oxidation	2.850	2.364	1.984

Supplementary S4: Discussion on thermoelastic damping (TED)

For studying the thermoelastic damping (TED) of a deformable solid beam proposed by Zener and modified by Lifshitz [8-10], the internal friction is defined in terms of the thermoelasticity of the material, thermal relaxation time, and angular frequency of the applied oscillation as

$$Q^{-1} = \tan\delta = \frac{E\alpha^2 T_0}{C_p}\frac{\omega\tau}{1+(\omega\tau)^2}, \tag{6}$$

where E, α, C_p, T_0, and ω are the Young's modulus, thermal expansion coefficient, heat capacity of the material per unit volume, mean temperature, and the angular frequency of the oscillation, respectively. The thermal relaxation time τ is given as,

$$\tau = \frac{C_p d^2}{\kappa\pi^2}, \tag{7}$$

where d is the width of the solid beam under oscillations and κ is the thermal conductivity of the oscillating solid. Under certain conditions, the internal friction exhibits the following proportionalities.

$$\begin{aligned} Q^{-1} &\propto \omega\tau \propto \kappa^{-1} \qquad \omega\tau \ll 1 \\ Q^{-1} &\propto \frac{1}{\omega\tau} \propto \kappa \qquad \omega\tau \gg 1 \end{aligned}. \tag{8}$$

In addition, TED depends on the scale of beam characteristic length and cross section d (Eq.(7)).

The decrease in the correlation factor of the BNNT–PEEK interface (Fig. 3(e)) indicates enhanced phonon scattering by the defects in the BNNTs; hence, it can be reasonably conjectured that the thermal conductivity of the nanocomposites decreases as vacancies and oxidation defects are introduced in the BNNTs. To understand the effect of the decreased thermal conductivity of the nanocomposites on their internal friction, the loss tangent was determined using Eq. (6) for various thermal conductivities and widths (d) of the composite beam. As shown in Fig. S4-1, the loss tangent decreases as the thermal conductivity increases

when the beam characteristic length is below 10^{-6} m. However, the loss tangent is proportional to thermal conductivity when the beam width is in the millimetre scale. Therefore, the increased

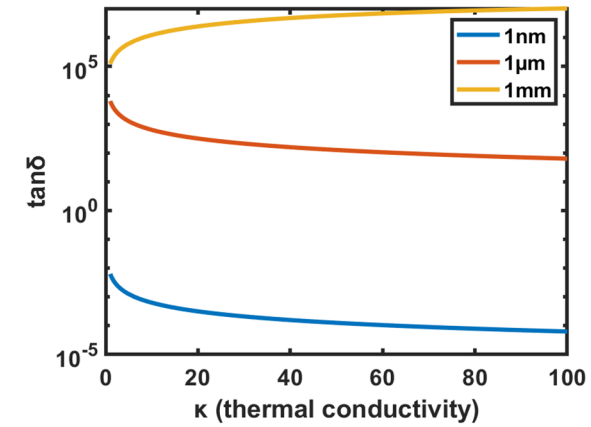

(a)

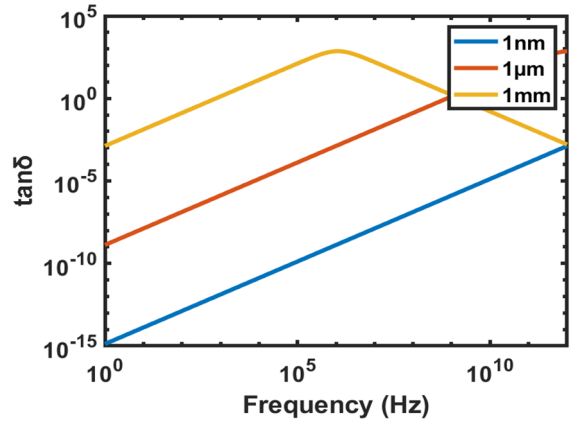

(b)

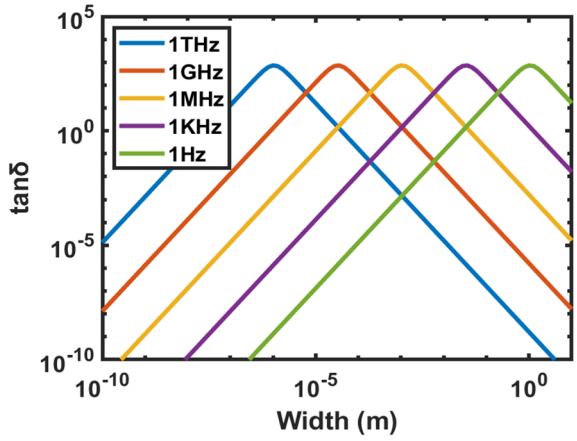

(c)

Fig. S4-1. Variations in the loss tangent of a beam under TED: (a) Effect of beam width and thermal conductivity and (b–c) Effect of applied angular frequency and beam width.

loss tangent of the BNNT/PEEK nanocomposites (Fig. 2(g)) could be due to both mechanical and thermal imperfections. Even though the size of the nanocomposite unit-cell considered in this study was below 1 nm, all periodic boundary conditions were applied. Therefore, it remains unclear whether the observed defect-induced behaviours are due to the compensatory or synergistic effects of the mechanical and thermal imperfections. The loss-tangent variations with angular frequency and beam width are also provided in Fig. S4-1.

References

[1] Senftle, T., Hong, S., Islam, M. et al. The ReaxFF reactive force-field: development, applications and future directions. npj Comput Mater, 2 (2016) 15011.

[2] Aditya Lele, Predrag Krstic, and Adri C. T. van Duin, ReaxFF Force Field Development for Gas-Phase hBN Nanostructure Synthesis, J. Phys. Chem. A, 126(4) (2022) 568–582.

[3] Evans, D. J. & Holian, B. L. The Nose-Hoover thermostat. J. Chem. Phys. 83 (1985) 4069–4074.

[4] H. J. C. Berendsen, J. P. M. Postma, W. F. van Gunsteren, A. DiNola, and J. R. Haak, Molecular dynamics with coupling to an external bath, J. Chem. Phys. 81 (1984) 3684.

[5] S Yang, S Yu, J Ryu, JM Cho, W Kyoung, DS Han, M Cho. Nonlinear multiscale modeling approach to characterize elastoplastic behavior of CNT/polymer nanocomposites considering the interphase and interfacial imperfection, Int. J. Plasticity, 41 (2013) 124-146.

[6] JL Tsai, SH Tzeng, YT Chiu. Characterizing elastic properties of carbon nanotubes/polyimide nanocomposites using multi-scale simulation. Composites Part B, 41 (2010) 106-115.

[7] Saeed Herasati, L.C. Zhang, H.H. Ruan, A new method for characterizing the interphase regions of carbon nanotube composites, International Journal of Solids and Structures, 51(9) (2014) 1781-1791.

[8] C Zener. Internal friction in solids: I. Theory of internal friction in reeds. Physical Review 52 (1937) 230-235.

[9] C Zener. Internal friction in solids: II. General theory of thermoelastic internal friction. Physical Review 53 (1938) 90-99.

[10] R Lifshitz, ML Roukes. Thermoelastic damping in micro- and nanomechanical systems. Physical Review B 61(8) (2000) 5600-5609.